

# Kent Academic Repository

## Full text document (pdf)

### Citation for published version

Harriss, K.H. and Burchell, Mark J. (2016) A study of the observed shift in the peak position of olivine Raman spectra as a result of shock induced by hypervelocity impacts. *Meteoritics and Planetary Science*, 51 (7). pp. 1289-1300. ISSN 1086-9379.

### DOI

<https://doi.org/10.1111/maps.12660>

### Link to record in KAR

<http://kar.kent.ac.uk/55423/>

### Document Version

UNSPECIFIED

#### Copyright & reuse

Content in the Kent Academic Repository is made available for research purposes. Unless otherwise stated all content is protected by copyright and in the absence of an open licence (eg Creative Commons), permissions for further reuse of content should be sought from the publisher, author or other copyright holder.

#### Versions of research

The version in the Kent Academic Repository may differ from the final published version.

Users are advised to check <http://kar.kent.ac.uk> for the status of the paper. **Users should always cite the published version of record.**

#### Enquiries

For any further enquiries regarding the licence status of this document, please contact:

[researchsupport@kent.ac.uk](mailto:researchsupport@kent.ac.uk)

If you believe this document infringes copyright then please contact the KAR admin team with the take-down information provided at <http://kar.kent.ac.uk/contact.html>

# A study of the observed shift in the peak position of olivine Raman spectra as a result of shock induced by hypervelocity impacts

**Kathryn H. Harriss**<sup>1</sup> and M. J. Burchell<sup>1</sup>

<sup>1</sup> School of Physical Sciences, University of Kent, Canterbury, Kent, CT2 7NZ.

Email: k.mcdermott@kent.ac.uk

## Abstract

Kuebler et al. (2006) identified variations in olivine Raman spectra based upon the composition of individual olivine grains, leading to identification of olivine composition from Raman spectra alone. However, shock on a crystal lattice has since been shown to result in a structural change to the original material, which produces a shift in the Raman spectra of olivine grains compared with the original un-shocked olivine (Foster et al., 2013). This suggests that the use of the compositional calculations from the Raman spectra, reported in Kuebler et al. (2006), may provide an incorrect compositional value for material that has experienced shock. Here we have investigated the effect of impact speed (and hence peak shock pressure) on the shift in the Raman spectra for San Carlos olivine (Fo<sub>91</sub>) impacting Al. foil. Powdered San Carlos olivine (grain size 1 to 10  $\mu\text{m}$ ) was fired at a range of impact speeds from 0.6 – 6.1  $\text{km s}^{-1}$  (peak shock pressures 5 – 86 GPa) at Al. foil to simulate capture over a wide range of peak shock pressures. A permanent change in the Raman spectra was found to be observed only for impact speeds greater than  $\sim 5 \text{ km s}^{-1}$ . The process that causes the shift is most likely linked to an increase in the peak pressure produced by the impact, but only after a minimum shock pressure associated with the speed at which the effect is first observed (here 65 – 86 GPa). At speeds around 6  $\text{km s}^{-1}$  (peak shock pressures  $\sim 86 \text{ GPa}$ ) the shift in Raman peak positions is in a similar direction (red shift) to that observed by Foster et al. (2013) but of twice the magnitude.

## Key words

Impact-cratering, Spectroscopy-Raman, Shock, olivine, Stardust

## 1. Introduction

The mineral olivine is one of the most abundant minerals in the solar system and forms a major component of asteroids, comets (Zolensky *et al.*, 2008) and dust particles (Henning, 2010). Olivine minerals range in composition depending on the Mg and Fe content within the formula  $(\text{Mg}, \text{Fe})_2[\text{SiO}_4]$ , with the end members being Fayalite  $(\text{Fe})_2[\text{SiO}_4]$  and Forsterite  $(\text{Mg})_2[\text{SiO}_4]$ . Previous studies of olivine minerals using Raman spectroscopy, have shown that the typical olivine spectra is dominated, and easily identifiable, by two close peaks with peak positions of around  $820 \text{ cm}^{-1}$  for peak 1 (P1) and  $850 \text{ cm}^{-1}$  for the second peak (P2) (Fig. 1) (e.g. Paques-Ledent and Tarte, 1973; Ishii, 1978; Piriou and McMillian, 1983; Guyot *et al.*, 1986; Chopelas, 1991; Mohanan *et al.*, 1993; Keubler *et al.*, 2006). The olivine peak doublet represents the internal stretching vibrational modes of the  $\text{SiO}_4$  ionic group) and the height of P1 and P2 are a function of the crystal orientation (Chopelas, 1991). However, it has been observed that the position of these peaks systematically varies with olivine composition, thus allowing compositional analysis of the olivine to be undertaken using Raman spectroscopy alone (e.g. Kuebler *et al.*, 2006, Ishibashi *et al.*, 2012). In general, the P1 and P2 twin peak structure has previously been shown to persist at static pressures up to 50 GPa. A systematic shift in position with increasing static pressure was reported, but this shift was reversed under relaxation to ambient conditions (Durben *et al.*, 1993). However, the shock induced within a crystal structure by hypervelocity impacts has been shown to cause a permanent shift in the P1 and P2 peak positions of olivine from that of the original unaltered olivine grains (Foster *et al.*, 2013). This was in impacts on aluminium at a speed of  $6.1 \text{ km s}^{-1}$ . The peak shift observed as a result of hypervelocity impacts is thought to be a result of the SiO bond being compromised during the impact. This follows on from earlier work e.g. Farrell-Turner *et al.*, 2005, which, although they found no systematic shifts in Raman spectra of polycrystalline olivine up to shock pressures around 59 GPa, did report some effects such as peak broadening as well as the appearance of some extra Raman bands at high shock pressures; this suggests some change in structure was starting to occur. Xie *et al.*, 2001, also reported on shock experiment on olivine rich samples. They reported that at peak shock pressures of 83 GPa, the P1 and P2 Raman peaks both broadened and sometimes shifted slightly to lower wave numbers, but provided no detailed quantitative analysis of this effect.

The work of Foster *et al.*, 2013, was stimulated by the way the NASA Stardust spacecraft collected cometary dust in space. The Stardust mission collected dust from comet 81P/Wild 2 in 2004 and returned it to Earth in 2006 (Brownlee *et al.*, 2006). This material was captured in silica aerogel and in craters on Al. foils, after an impact at  $6.1 \text{ km s}^{-1}$ , which occurred as the spacecraft flew past the comet and was struck by the freshly ejected cometary dust. Analysis of these materials has provided insights into the composition of the comet, which, amongst other things, contained crystalline silicates consisting of a mixture of pre-solar and solar materials (e.g., Keller *et al.*, 2006; Wopenka, 2012; Floss *et al.*, 2013). The particles captured in aerogel are distributed as terminal grains in tracks, or as fine grained material along the walls of the tracks, and have a highly varied shock pressure history due to the capture method (e.g. see Hörz *et al.*, 2006; Burchell *et al.*, 2008a) with peak shock pressures estimated as  $\sim 800 \text{ MPa}$  (e.g. Trigo-Rodriguez *et al.*, 2008). By contrast, cometary dust impacts at  $6.1 \text{ km s}^{-1}$  on the Al. foils resulted in classic bowl shaped craters or multiple pit craters (e.g., Hörz *et al.*, 2006; Kearsley *et al.*, 2009; Price *et al.*, 2010) which contained most of the impactor retained in a single location. The hypervelocity impacts that formed the crater within the Al. foil would have caused the olivine grains to experience peak shock pressures estimated as 85-90 GPa for  $\text{Fo}_{90}$  (at  $6.1 \text{ km s}^{-1}$ , Burchell and Kearsley, 2009), or 79 GPa for  $\text{Fo}_{89}$  (at  $5.82 \text{ km s}^{-1}$ , Wozniakiewicz *et*

*al.*, 2012a). The peak shock pressure range indicated by these estimates (some 80 – 90 GPa depending on the estimate used) is sufficient to cause at least partial melting of the projectile material, forming a melt residue within the crater (e.g. see Bernard and Hörz, 1995). However, Wozniakiewicz *et al.*, 2012b, showed that the crystalline silicate material present in these craters arose directly from the original impactor and not from a recrystallized melt (also see Burchell *et al.*, 2008b).

Whilst this picture of (relatively) intact cometary grains being preserved in the Stardust aerogel, vs. heavily processed (melted or fragmented) grains being found in the Al. foil, suggests that the former is favoured for analysis; this is not quite the full picture. For example, Bernard and Hörz *et al.*, 1995, reported that even in impacts of glass on Al. at  $7 \text{ km s}^{-1}$  there was some un-melted projectile material in the crater afterwards. Similarly, Hernandez *et al.*, 2006, showed that impacts of metallic projectiles on metal targets at speeds up to  $5 \text{ km s}^{-1}$ , produced not just impact melt but discrete fragments of the impactor in the crater walls. Subsequently, it was shown by Burchell *et al.*, 2008b, that not only were distinct fragments of several mineralic impactors on Al. foil detectable lining the crater after impact at  $6.1 \text{ km s}^{-1}$ , but that they had also preserved sufficient crystallinity to be identifiable by Raman spectroscopy. Later work has studied such craters in detail and shown that the fragments can comprise a relatively large fraction of the original grain, particularly for small impactors (e.g., see Wozniakiewicz *et al.*, 2012b, Croat *et al.*, 2015). However, the capture process may have left residual strain in the crystalline lattice. Accordingly, Foster *et al.*, 2013, investigated the effects of high speed capture of olivine grains into aerogel and aluminium foils for a suite of Mg-Fe compositions. They fired synthetic olivine into aerogel and Al. foils at speeds of  $\sim 6.1 \text{ km s}^{-1}$ . The material captured within the resulting aerogel tracks and Al. foil craters was analysed using Raman spectroscopy and the spectra then compared to that of the original un-shot olivine grains to determine the effect of impact on the position of P1 and P2 peaks. Their most significant conclusion was that for highly shocked olivine material captured in the Al. foils, there was a change in the relationship between the positions of the two main Raman olivine peaks P1 and P2 as a result of the strain imposed on the olivine crystal lattice during the impact event. Therefore, cometary dust residue located in the Al. foils on the Stardust mission and analysed by Raman spectroscopy, would not give a true result for the olivine composition, unless this bias was corrected.

However, the work undertaken by Foster *et al.* (2013) was limited in that: (1) The olivine grains making the impact craters were single grains,  $10 - 12 \text{ }\mu\text{m}$  in size. In the cometary dust collected by Stardust, grains of this size were often assemblages of much finer grained material of varying compositions, and the majority of impacts were made by impactors smaller than  $10 \text{ }\mu\text{m}$ . (2) The synthetic olivine material used by Foster *et al.* (2013) contained some unreacted ingredients which may potentially have had an unknown effect on the Si-O vibrational state. (3) The data were collected at a single impact speed and thus provide little insight into how the results vary with impact speed and thus peak shock pressure.

Accordingly, this paper investigates the Raman spectra of micrometre scale olivine powder which impacted Al. foil at a range of velocities and thus peak pressures. The material used for this investigation was natural homogenous San Carlos Olivine material, removing the possible effect of unreacted materials in artificial olivine. The olivine was ground into small grains with a significant fraction smaller than  $10 \text{ }\mu\text{m}$ .

## 2. Method

Milligrams of sub-micrometre San Carlos olivine powder were loaded into a nylon discarding-sabot and fired at 1 cm<sup>2</sup> pieces of 103 µm thick Stardust analogue Al. foil (Al. 1080), using the two stage light gas gun at the University of Kent (Burchell *et al.*, 1999). In total, six shots were undertaken, with impact speeds ranging from 0.6 to 6.3 km s<sup>-1</sup> (Table 1). The speed for each shot was measured using sensors which detected the time of exit from the launch tube, the impact of the sabot on a plate placed part way down the range and the impact on the target. This gave a shot speed accurate to ±4% for small (<5 micron) projectiles, with the size of the uncertainty dominated by dispersion of the fine dust into a cloud during the shot. The target was arranged perpendicular to the line of flight, so all impacts were at normal incidence.

The peak shock pressure in each shot was calculated using the Planar Impact Approximation, PIA, (Melosh, 1989), with a linear wave speed equation with S and C values of 0.88 and 6.0 kms<sup>-1</sup> for Fo<sub>92</sub> (Ahrens and Johnson, 1995) and of 1.34 and 5.380 kms<sup>-1</sup> for Al. 1100 (Marsh, 1980). The olivine density was 3246 kg m<sup>-3</sup>, with 2712 kg m<sup>-3</sup> for Al. The resulting peak pressures are given in Table 1. At the higher speed of 6.31 km s<sup>-1</sup>, the calculated peak shock pressure generated during impact is 86.1 GPa, which is within the range give previously by Burchell and Kearsley, 2009. If we recalculate the PIA at an impact speed of 5.82 km s<sup>-1</sup>, the speed used by Wozniakiewicz *et al.*, 2012a, we find a peak pressure of 77.1 GPa, comparable to the value of 79 GPa reported by Wozniakiewicz *et al.*, 2012a.

The olivine powder used was a natural San Carlos olivine from Arizona, which has been used in previous work (e.g. Kearsley *et al.* 2007; 2009) and which was subject to a range of analytic tests to confirm its nature. Wozniakiewicz *et al.*, 2009, used SEM-EDX analysis on this sample to confirm it as Fo<sub>91</sub> compatible with the generally reported range of values for San Carlos olivine reported in the literature (e.g. see Fournelle, 2007). The raw grains were reduced in size using a Retsch PM 100 ball mill at the University of Kent. The first step was dry milling to reach sizes > 10 µm. This was followed by wet milling to achieve sizes of < 10 µm. An SEM image of the grains is shown in Fig. 2, and typical sizes ranged from <1 to 10 µm with the majority (>50%) of the grains being <5 µm.

During a shot, the powdered projectile material formed a cloud which impacted the Al. foil forming craters. After each shot, the Al. foils were studied using a scanning electron microscope (Hitachi S3400N). All the images were obtained without a carbon coating, using an operating voltage of 20 kV and an emission current between 75-90 nA. An Oxford instrument EDX system (XMAX-80 Silicon drift detector) was used to confirm that the craters contained silicate residue, and to produce a high magnitude map of the foil. The presence of large craters in some shots however, implies impactors above the size limit of the samples during preparation; it suggests that some of the fine grains clumped together during handling and remained so during flight in the gun. This would have produced assemblages which were multi-grained objects at the moment of impact, and hence larger craters. In Fig. 3, we show a montage of images of craters from the high speed shots. The number of craters increases with increasing impact speed with 2287 craters observed after the impact speed of 1.09 kms<sup>-1</sup> and >10,000 craters observed at 6.31 kms<sup>-1</sup>. This combined with the greater frequency of larger craters in the low speed shots suggests that these multi-grained assemblages were more likely to break up under the shock of being fired at higher speeds resulting in more numerous small craters.

The target foils were then analysed via Raman spectroscopy, using a red (633nm) laser with a grating of 600 lines per mm on a Horiba LabRam-HR Raman spectrometer with a maximum laser power of ~3 mW at the sample, thus avoiding unwanted heating and possible modification of the sample material. The laser spot size was typically a few  $\mu\text{m}$  diameter. The presence of olivine was easily identifiable due to the distinct doublet peak with main peaks P1 and P2 (Fig. 1). In total, Raman spectra were taken from 40 raw grains spectra (some before and after every shot). From these spectra, for the raw grains, we obtained  $P1 = 823.80 \pm 0.12$ ,  $\sigma = 0.68$ ,  $\text{cm}^{-1}$ , and  $P2 = 856.01 \pm 0.16$ ,  $\sigma = 0.90$ ,  $\text{cm}^{-1}$ . The value of  $\sigma$  given is the standard deviation of the sample about the mean. Note that the uncertainty given on each mean value is the error on the mean, assuming a standard distribution and taking the uncertainty as  $\sigma/n$  (where  $n$  is the number of spectra used). These mean values correspond to an olivine composition of  $\text{Fo}_{84.5}$  (P1) and  $\text{Fo}_{87.3}$  (P2) using equations 1 and 2 respectively from Foster et al. (2013). Both values are lower than expected from the SEM-EDX compositional analysis and for high Fo values are estimated by Foster et al. (2013) to be accurate to 1.7 molar units. Foster et al. (2013) also provide a calibration for the Fo content in terms of the difference  $P2-P1$ , and this (eqn. 3) gives  $\text{Fo}_{96.0}$ , but at high Fo values this estimate is uncertain to 5 molar units.

### 3. Results

In this section we discuss the results shot by shot. We describe the crater sizes and shape. Inside each shot, Raman spectra were taken from 4 – 15 craters. The results and standard deviation ( $1\sigma$ ) of the mean values for the P1 and P2 peak positions are shown in Table 1. Details of the crater morphology (Fig. 3) and the Raman results from the residues (Fig. 4, vs. impact speed, and Fig. 5, vs. peak shock pressure) in all shots are given below. **Figure 6 shows the mean spectra for all shots and the unshot olivine to show the shift in P1 and P2 peak position with increasing impact speed. Mean spectra were formed by co-adding all individual spectra inside each shot.**

#### 3.1 Impact speed $0.60 \text{ km s}^{-1}$

At the slowest speed of  $0.6 \text{ km s}^{-1}$ , we found few well defined craters on the surface of the Al. foil, due to the low speed of the impacting grains. Although we had hoped some grains might have stuck in the foils, the few craters that were observed were  $<10 \mu\text{m}$  in diameter and produced carbon rich Raman spectra, suggesting they arose from impact of some sort of gun debris. We thus suggest that at this speed the grains rebounded from the foil after impact (rather than embedding themselves or making impact craters). Given the small size of the grains we were unable to recover the grains from the floor of the target chamber after the impacts. Further, given the lack of craters there were no Raman spectra after impact from this shot.

#### 3.2 Impact speed $1.09 \text{ km s}^{-1}$

In this shot the craters were few and far between, with the majority being very small  $<10 \mu\text{m}$  (94 %) with only 2 craters being larger than  $50 \mu\text{m}$ . The craters were round and bowl shaped with a rounded lip around the entire length of the circumference. There appeared to be little elongation or butterfly symmetry to the lip and crater rim. One crater (dia. =  $20.2 \mu\text{m}$ , see Fig 3A “single crater”) appeared to have the projectile sticking out of the foil, indicating intact capture of the projectile which had embedded itself in the foil. Some silicate rich material from the projectiles was observed in places on the surface of the foil in large clumps without having produced an observable impact

crater. This clumping effect would explain the lack of smaller craters as the large clumps will contain much of mass of the projectile material.

Four craters were found to contain olivine peaks within the Raman spectra of the crater residue. All four craters were  $<20\ \mu\text{m}$  in diameter, and it was the four largest crater in this size range which gave olivine Raman spectra. Due to the small size of these craters, only one Raman analysis was recorded from each. A strong carbon signal both the G and D bands were also observed within the crater residue spectra, indicating that a fine layer of gun debris had also reached the target after the olivine and been preserved. The crater residue produced at this speed show a slight positive shift (defined as being to higher wave numbers) in both the P1 and P2 positions ( $824.35 \pm 0.10$ ,  $\sigma = 0.20$ ,  $\text{cm}^{-1}$  and  $856.64 \pm 0.07$ ,  $\sigma = 0.13$ ,  $\text{cm}^{-1}$  respectively) compared to the un-shot grains ( $823.80 \pm 0.12$ ,  $\sigma = 0.68$ ,  $\text{cm}^{-1}$  and  $856.01 \pm 0.16$ ,  $\sigma = 0.90$   $\text{cm}^{-1}$  respectively). This was the only shot where the residue showed a positive shift in peak positions (see Figs. 4, 5 and 6). It should be noted however, that this shift is only just three times the error on the value, with therefore borderline statistical significance. We also considered if the peak positions were varying in a common way by forming the difference in mean peak positions (P2 – P1, see table 1). The P2-P1 value in this, and indeed in all the shots, remains fairly constant around  $32\ \text{cm}^{-1}$ , which is similar to that observed in the raw grains as well.

### **3.3 Impact speed $1.90\ \text{kms}^{-1}$**

The craters that were observed in this foil were elongated with uneven crater lips which side the longest diameter. They were shallow with short crater walls and easily observable crater floors, within which residue is observed in the larger craters ( $20\text{-}50\ \mu\text{m}$ , 12 % of the observed craters). Only three large craters were observed  $>50\ \mu\text{m}$ . With one exception, at this size the craters still appeared elongated on one axis, and therefore produced a butterfly-like symmetry along the long edge of the crater (see examples in Fig 3B). Unlike the impacts at  $1.09\ \text{km s}^{-1}$ , the craters did not contain large intact impactors, but did show considerable material retained at the impact site. Some of the smallest craters ( $<10\ \mu\text{m}$ , 50 %) do not show the elongated feature, instead having the rounded bowl shape crater appearance characteristic of hyper velocity impacts, similar to those observed in the higher speed studies. This foil appears to have a greater density of gun debris, all of which has a high carbon composition but was readily identifiable from the mineralic cratering.

Individual Raman spectra from 15 different craters of  $50\text{-}100\ \mu\text{m}$  in diameter were analysed. The mean P1 position shows a negative shift of  $0.4\ \text{cm}^{-1}$ , with the mean P2 peak position having a negative shift of  $1.15\ \text{cm}^{-1}$ . The shift in P1 mean has low significance when the associated error is considered (see Figs. 4a, 5a and 6, where the error bars are shown). The shift in P2 does appear more significant, but when the data for all shots is looked at no trend emerges at this speed indicating that it is a fluctuation rather than a physical phenomenon.

### **3.4 Impact speed $4.00\ \text{kms}^{-1}$**

The craters produced at this speed had a rounded appearance with irregular lip features around the edge (Fig. 3C). There were multiple small craters  $\leq 10\ \mu\text{m}$  (93 % of total craters) that had similar profiles to that observed in the larger craters, i.e. a bowl shape with a raised lip around the complete rim of the crater; the larger craters did however appear to show more irregular lip features. Some larger irregular material exists on the surface of the foil. However from the SEM analysis this material had no Si and a high C content. It is therefore debris from the firing process and was

ignored. Some of the larger craters  $>20\ \mu\text{m}$  (2 % of total) had irregular crater lips that were not uniform and had a butterfly-like symmetry.

Analysis of the impact residue in 10 craters demonstrated a negative shift in the peak position of both of the P1 and P2 peaks by  $0.20\ \text{cm}^{-1}$  and  $0.16\ \text{cm}^{-1}$  respectively when compared to that of the original raw olivine grains (Figs. 4, 5 and 6). However, compared to the uncertainties in the results (the error bars are shown in Figs. 4, 5 and 6), the data are readily compatible with no statistically significant shift being observed.

### **3.5 Impact speed $5.12\ \text{kms}^{-1}$**

The craters at this speed were numerous with more than 5000 craters being observed, 97 % of which were  $<10\ \mu\text{m}$  in diameter. The craters were all rounded bowl shaped with irregular lips (Fig. 3D) around the crater. Many of the craters produced an olivine Raman spectrum in the Raman spectrometer, in addition to a strong Mg peak when analysed on the SEM-EDX. There were not a large number of craters larger than  $20\ \mu\text{m}$  in diameter with the largest observed being  $38\ \mu\text{m}$ . A large crater near the centre of the foil, was produced by gun debris travelling at around  $2\ \text{kms}^{-1}$ . There was no evidence of any crater containing large fragments of intact projectile material.

10 craters were analysed from the foil impact at  $5.12\ \text{km s}^{-1}$ ; all produced strong olivine peak doublets. This experiment was completed at a later date compare to the others recorded here and thus used a differing sample of San Carlos olivine. Therefore the Raman spectra of the crater residues from this shot were compared to raw grains of the new sample, rather than the mean of the raw olivine powder used previously. The mean P1 and P2 positions on ten Raman spectra from the new sample of the raw olivine powder were found to be  $824.2 \pm 0.1$ ,  $\sigma = 0.2$ ,  $\text{cm}^{-1}$  and  $856.4 \pm 0.1$ ,  $\sigma = 0.4$ ,  $\text{cm}^{-1}$  respectively. These suggest Fo values of  $\text{Fo}_{87.3}$  and  $\text{Fo}_{89.2}$  respectively, or  $\text{Fo}_{95.9}$  from P2-P1, using the calibrations of Foster et al., 2013. These are in general compatible with the expected value of  $\text{Fo}_{91}$ .

The mean P1 and P2 values for the crater residues show a negative shift (Figs. 4, 5 and 6) for the P1 and P2 peak positions. The degree of shift ( $-0.39$  for P1 and  $-0.47$  for P2) still falls just within one error bar of no shift at all, again indicating that the shift is not significant, even at a high impact shock pressure of 65 GPa (Fig. 5).

### **3.6 Impact speed $6.31\ \text{kms}^{-1}$**

The craters on this foil were numerous and ranged in diameter from  $<10\ \mu\text{m}$  to  $160\ \mu\text{m}$ , with only 1% of craters having a diameter  $>50\ \mu\text{m}$  and 77 % of craters having a diameter  $<10\ \mu\text{m}$ . A calibration has previously been obtained for crater diameter vs. projectile diameter at an impact speed of  $6.1\ \text{km s}^{-1}$  (Kearsley et al., 2007). Ignoring the slight difference in speeds, this suggests that for crater diameters of 10 and  $50\ \mu\text{m}$ , the olivine impactor size was 2 and  $10\ \mu\text{m}$  respectively. The crater sizes in general in this shot are thus compatible with the raw grain size distribution. A later re-calibration (at similar speed) for projectiles of less than  $10\ \mu\text{m}$  dia., suggested that at smaller sizes a slightly different calibration holds, due to a strain-rate dependence in the target strength (Price et al., 2010). However, this would predict here an impactor size range of 5 and  $10\ \mu\text{m}$  dia. for crater diameters of 10 and  $50\ \mu\text{m}$  dia. respectively, still compatible with the raw grain size distribution.



Given the calibration of Price et al. (2010), this suggests that only 1 % of impactors had a diameter > 50  $\mu\text{m}$ , whilst 77 % of impactors had a diameter of 10  $\mu\text{m}$  or less. The increased number and frequency of small craters <10  $\mu\text{m}$  (compared to that in lower speed shots, where normally higher speed shots of the same material usually produce larger craters) suggests that the greater acceleration allows any aggregated projectile material to separate into the finely milled powder sized components. This also explains the greater number of craters overall in the higher speed shots.

The small craters were all rounded with crater lips which continued around the length of the crater rim. The crater walls and floor were not observed in the images suggesting that they were relatively deep. The crater lips are similar in length to the radius of the craters they surround. In several of the larger craters it was possible to observe the crater floor using SEM imaging, which had a mosaic texture which is the residue of the projectile (Fig 5E), this texture is discussed in detail in Wozniakiewicz et al., 2015.

In this shot we obtained 9 Raman spectra from 9 of the small craters. The impact residue had a mean P1 peak position of  $821.95 \pm 0.21$ ,  $\sigma = 0.62$ ,  $\text{cm}^{-1}$ , a lower wave number than the raw unaltered grains by  $1.85 \pm 0.24$   $\text{cm}^{-1}$  (Figs. 4, 5 and 6). The same direction of shift is also observed for the mean P2 position (average peak position of  $853.96 \pm 0.21$ ,  $\sigma = 0.63$ ,  $\text{cm}^{-1}$ ), with an average difference between the crater residue and the raw un-altered grains of  $2.05 \pm 0.18$   $\text{cm}^{-1}$ . This was the only shot where both P1 and P2 seemed to have undergone a shift in value of statistical significance (Fig. 6). The difference between the P1 and P2 peak positions ( $P2 - P1$ ) was however constant at around 32  $\text{cm}^{-1}$ .

## 4. Discussion

### 4.1 Variation in crater morphology with velocity speed

The variation in crater morphology with impact speed, for impacts on aluminium has been reported in great detail by previous researchers. For example, Bernard and Hörz, (1995), describe how crater shape varies for impacts of soda lime glass spheres (dia. 3.2 mm) impacting aluminium 1100 at speeds from 1 to 7  $\text{km s}^{-1}$ . The data here overlap substantially with the impact speed regime of Bernard and Hörz, (1995), but do so with projectiles some 3 orders of magnitude smaller in diameter. As pointed out by Price et al. (2013), strain rate hardening can influence the size of micrometre scale craters when high strain rates are achieved in impacts.

Whilst in this paper we present no detailed depth to diameter measurements of crater shape, the evolution of crater shape with impact speed does show some trends. We note that crater morphology and depth do appear to vary with increasing impact speed. For example, the crater shapes typically observed in the 1.09  $\text{kms}^{-1}$  shot were elongated and shallow with butterfly crater lips along the long axis. The crater walls were not steep, with the crater floor being visible in the small craters (<20  $\mu\text{m}$ ). In some cases the projectile actually remained intact within the crater (extruding from the foil due to the shallowness of the crater). The craters produced in the 1.9  $\text{kms}^{-1}$  shot were similar, but with less evidence of projectile capture. By contrast, the impacts in the 4  $\text{km s}^{-1}$ , 5.12  $\text{km s}^{-1}$  and 6.3  $\text{km s}^{-1}$  shots produced deep bowl shaped craters with irregular lips and steep crater walls. This transition from low speed craters to those more typical of hypervelocity impacts thus occurs at speeds between around 2 and 4  $\text{km s}^{-1}$ , as also reported for larger craters by Bernard and Hörz,

1995. Thus whilst (relative) crater size may be influenced by strain rate effects in micrometre scale impacts, the general evolution of crater shape with impact speed is not.

#### **4.2 Residue in craters.**

The earlier work of Bernard and Hörz (1995) not only describes the evolution of crater shape with impact speed, but also the distribution of projectile material inside the crater. They note, as here, the increasingly fragmented nature of the material, along with the on-set of the appearance of melted material as impact speed increases. They rely on appearance in images to indicate the presence of melt, but do report seeing un-melted fractions even at impact speeds of up to  $7 \text{ km s}^{-1}$ . A more detailed TEM study of projectile residues is reported in Wozniakiewicz et al., 2012a,b, where the presence of un-melted material after impacts of minerals into Al. at around  $6 \text{ km s}^{-1}$  is extensively reported. There is a separate TEM study of residue in impact craters in Al. at  $6 \text{ km s}^{-1}$  in Croat et al., 2015. All the authors seem to agree that significant amounts of projectile material remain in the craters even at high impact speeds. What the work reported here also shows, is that subtle changes in structure may still be occurring at high impact speed, even when the material appears intact in terms of composition and morphology.

#### **4.3 Comparison of the Raman results with past work**

Foster et al. (2013), undertook similar experiments to those here firing monolithic olivine grains at Al. foil targets, but used a single impact speed ( $\sim 6.1 \text{ km s}^{-1}$ ) and olivine grains of three well constrained Fo compositions ( $\text{Fo}_{40}$ ,  $\text{Fo}_{80}$  and  $\text{Fo}_{100}$ ). Foster et al. (2013) carried out Raman spectroscopy on the resulting residues in impact craters with diameters around  $50 \text{ }\mu\text{m}$  (corresponding to impacts by grains around  $10 - 12 \text{ }\mu\text{m}$  in diameter). They concluded that for olivine with Fo compositions of 40, 80 and 100, a shift in the olivine P1 and P2 Raman peak positions occurred, producing lower peak positions for the residue than those of the original raw grains. It was observed that the shift was dependent on the Fo composition with a greater shift observed for  $\text{Fo}_{100}$  ( $1 \text{ cm}^{-1}$ ) than that observed for  $\text{Fo}_{40}$  ( $0.5 \text{ cm}^{-1}$ ) for P1. The position of P2 also shifted downwards with the opposing trend of a greater shift at lower Fo compositions. There was thus a change in P2-P1 which depended on Fo composition. The shifts observed here are in the same direction as those of Foster et al., 2013, but are larger in size (by a factor of about 2) and are of equal magnitude for both P1 and P2.

Given that a separate study of impact residues by Wozniakiewicz et al., 2012a had shown, via SEM-EDZ analysis, that there was no significant change in elemental composition of the olivine as a result of the impact and that the crystalline fragments in the residue had retained their original crystallinity (and were not recrystallized melt), Foster et al. (2013), concluded that the shift in the Raman peaks was a result of strain introduced into the samples by the impact shock. However, they only worked at one impact speed and hence shock pressure, so did not establish if this effect was simply proportional to impact shock pressure, or, if as reported for static loading by Durben et al. (1993), any such effect was reversed on unloading until a critical threshold (50 GPa) was passed. Independent of this subtlety, Foster et al. (2013) concluded that determining olivine molar composition from the P1 and P2 Raman peak positions (e.g. using equations 1, 2 and 3 given in Kuebler (2006)) can only strictly be applied to un-shocked samples. They then observed that olivine impact residues collected from comet 81P/Wild-2 via impacts at  $6.1 \text{ km s}^{-1}$  onto Al. foils, and analysed for their Fo content by Raman spectroscopy (as reported by for example Wopenka, 2012)

will be mis-interpreted without an appropriate correction (a new calibration appropriate to impacts at  $\sim 6 \text{ km s}^{-1}$  was supplied by Foster *et al.*, 2013).

## 5. Conclusions

The results from this study confirm those of Foster *et al.*, 2013, concerning a downward (red) shift in olivine Raman spectra P1 and P2 peaks after a high pressure shock. We find that the change in Raman spectra peak positions for olivine after shock, only becomes permanent above peak shock pressures in the range 65 – 86 GPa. At lower impact shock pressures, any change which may occur during the shock is temporary and lost upon unloading. In static loading of olivine, Durben *et al.*, 1993, found no permanent change in the Raman spectra in experiments up to 50 GPa pressure. They did, however, note the appearance of new additional Raman peaks when samples were loaded above 30 GPa, indicating the on-set of a build-up of defects above 30 GPa. Similarly, earlier work on shock loading found indications of structural changes from around 40 GPa upwards (Xie *et al.*, 2001, Farrell-Turner *et al.*, 2005). We thus conclude that the change in positions of P1 and P2 observed here is due to an irreversible change in the olivine structure, either accumulation of defects or on-set of a structural rearrangement.

The shift we observe here in P1 and P2 peak positions is twice that reported by Foster *et al.*, 2013. This may be a result of the use here of smaller olivine grains as projectiles. Price *et al.*, 2010, observed that as impactor diameter fell below 10  $\mu\text{m}$  there was an abrupt reduction in crater size in impacts on Al. foil at  $6 \text{ km s}^{-1}$ . In a subsequent paper (Price *et al.*, 2013), they attribute this change to a rapid change in Al. strength as the strain rate increases. This effect is not included in the PIA calculations used here, so it may be that the peak shock pressure at  $6 \text{ km s}^{-1}$  is underestimated for small grain sizes below 10  $\mu\text{m}$ . A fully detailed hydrocode simulation using a strain-rate dependent strength model is required to explore this point further.

## Acknowledgements

We thank STFC (UK) for providing the funding for this study. We thank A. Kearsley and J. Hillier for supplying the San Carlos olivine and the experimental officer Mike Cole for aiding with the gun shots. We also thank the reviewers for their helpful comments.

## References

- Ahrens, T. J., and Johnson, M. L. 1995. Shock wave data for minerals. *Mineral Physics & Crystallography: A Handbook of Physical Constants*, 143-184.
- Bernard R. P., and Hörz F. 1995. Craters in aluminum 1100 by soda-lime glass spheres at 1 to 7 km/s. *Int. J. Impact Engng.*, 17, 69 – 80.
- Brownlee D. E., Tsou P., Aleón J., Alexander C. M. O'D., Araki T., Bajt S., Baratta G. A., Bastien R., Bland P., Bleuet P., Borg J., Bradley J. P., Brearley A., Brenker F., Brennan S., Bridges J. C., Browning N., Brucato J. R., Brucato H., Bullock E., Burchell M. J., Busemann H., Butterworth A., Chaussidon M., Chevront A., Chi M., Cintala M. J., Clark B. C., Clemett S. J., Cody G., Colangeli L., Cooper G., Cordier P. G., Daghlian C., Dai Z., D'Hendecourt L., Djouadi Z., Dominguez G., Duxbury T., Dworkin J. P., Ebel D., Economou T. E., Fairey S. A.J., Fallon S., Ferrini G., Ferroir T., Fleckenstein H., Floss C., Flynn G., Franchi I. A., Fries M., Gainsforth Z., Gallien J.-P., Genge M., Gilles M. K., Gillet P., Gilmour J., Glavin D. P., Gounelle M., Grady M. M., Graham G. A., Grant P. G., Green S. F., Grossemy F., Grossman L., Grossman J., Guan Y., Hagiya K., Harvey R., Heck P., Herzog G. F., Hoppe P., Hörz F., Huth J., Hutcheon I. D., Ishii H., Ito M., Jacob D., Jacobsen C., Jacobsen S., Joswiak D., Kearsley A. T., Keller L., Khodja H., Kilcoyne A. L. D., Kissel J., Krot A., Langenhorst F., Lanzirotti A., Le L., Leshin L., Leitner J., Lemelle L., Leroux H., Liu M.-C., Luening K., Lyon I., MacPherson G., Marcus M. A., Marhas K., Matrajt G., Meibom A., Mennella V., Messenger K., Mikouchi T., Mostefaoui S., Nakamura T., Nakano T., Newville M., Nittler L. R., Ohnishi I., Ohsumi K., Okudaira K., Papanastassiou D. A., Palma R., Palumbo M. O., Pepin R. E., Perkins D., Perronnet M., Pianetta P., Rao W., Rietmeijer F., Robert F., Rost D., Rotundi A., Ryan R., Sandford S. A., Schwandt C. S., See T. H., Schlutter D., Sheffield-Parker J. A., Simionovici S., Sitnitsky S. I., Snead C. J., Spencer M. K., Stadermann F. J., Steele A., Stephan T., Stroud R., Susini J., Sutton S. R., Taheri M., Taylor S., Teslich N., Tomeoka K., Tomioka N., Toppani A., Trigo-Rodríguez J. M., Troadec D., Tsuchiyama A., Tuzzolino A. J., Tyliszczak T., Uesugi K., Velbel M., Vellenga J., Vicenzi E., Vincze L., Warren J., Weber I., Weisberg M., Westphal A. J., Wirick S., Wooden D., Wopenka B., Wozniakiewicz P. A., Wright I., Yabuta H., Yano H., Young E. D., Zare R. N., Zega T., Ziegler K., Zimmerman L., Zinner E., Zolensky M. 2006. Comet 81P/Wild 2 under a microscope. *Science*, 314(5806), 1711-1716.
- Burchell, M. J. and Kearsley, A. T. 2009. Short-period Jupiter family comets after Stardust. *Planetary and Space Science*, 57(10), 1146-1161.
- Burchell, M. J., Cole, M. J., McDonnell, J. and Zarnecki, J. 1999. Hypervelocity impact studies using the 2 MV Van de Graaff accelerator and two-stage light gas gun of the University of Kent at Canterbury. *Measurement Science and Technology*, 10(1), 41.
- Burchell M. J., Fairey S. A. J., Wozniakiewicz P., Brownlee D. E., Hörz F., Kearsley A. T., See T. H., Tsou P., Westphal A., Green S. F., Trigo-Rodríguez J. M. and Domínguez G. 2008a, Characteristics of cometary dust tracks in Stardust aerogel and laboratory calibrations. *Meteoritics & Planetary Science* 43, 23–40.
- Burchell, M., Foster, N., Kearsley, A. and Creighton, J. 2008b. Identification of mineral impactors in hypervelocity impact craters in aluminum by Raman spectroscopy of residues. *Meteoritics & Planetary Science*. 43(1-2), 135-142.

- Chopelas, A. 1991. Single crystal Raman spectra of forsterite, fayalite, and monticellite. *Am. Mineral.* 76, 110L1109.
- Croat, T. K., Floss, C., Haas, B. A., Burchell, M. J., and Kearsley, A. T. 2015. Survival of refractory presolar grain analogs during Stardust-like impact into Al foils: Implications for Wild 2 presolar grain abundances and study of the cometary fine fraction. *Meteoritics & Planetary Science*, 50(8), 1378-1391.
- Durben D. J., McMillan P. F. and Wolf G. H. 1993 Raman study of the high pressure behaviour of forsterite (Mg<sub>2</sub>SiO<sub>4</sub>) crystal and glass. *Am. Min.* 78, 1143–1148.
- Farrell-Turner S., Reimold W.U., Nieuwoudt M., Erasmus R.M. 2005. Raman spectroscopy of olivine in dunite experimentally shocked to pressures between 5 and 59 GPa. *Meteoritics & Planetary Science* 40, 1311 – 1327.
- Floss C., Stadermann F. J., Kearsley A. T., Burchell M. J., and Ong W. J. 2013 The abundance of presolar grains in Comet 81P/Wild 2. *Astrophysical Journal* 763:140 (11 pages). doi:10.1088/0004-637X/763/2/140
- Foster N., Wozniakiewicz, P. J., Price, M. C., Kearsley, A. T. and Burchell, M. J. 2013. Identification by Raman spectroscopy of Mg–Fe content of olivine samples after impact at 6 km s<sup>-1</sup> onto aluminium foil and aerogel: In the laboratory and in Wild-2 cometary samples. *Geochimica et Cosmochimica Acta* 121, 1-14.
- Fournelle, J. 2007. Notes on Some Crystals of San Carlos Olivine and EPMA Standards. American Geophysical Union, Fall Meeting 2009, abstract #V31E-2009.
- Guyot, F., Boyer, H., Madon, M., Velde, B., and Poirier, J. P. 1986. Comparison of the Raman microprobe spectra of (Mg, Fe) <sub>2</sub> SiO <sub>4</sub> and Mg <sub>2</sub> GeO <sub>4</sub> with olivine and spinel structures. *Physics and Chemistry of Minerals*, 13(2), 91-95.
- Henning, T. 2010. Cosmic silicates. *Annual Review of Astronomy and Astrophysics* 48, 21-46.
- Hernandez V. S., Murr L. E., and Anchondo I. A. 2006. Experimental observations and computer simulations for metallic projectile fragmentation and impact crater development in thick metal targets. *International Journal of Impact Engineering* 32, 1981–1999.
- Hörsz F., Bastien R., Borg J., Bradley J. P., Bridges J. C., Brownlee D. E., Burchell M. J., Cintala M. J., Dai Z. R., Djouadi Z., Dominguez G., Economou T. E., Fairey S. A. J., Floss C., Franchi I. A., Graham G. A., Green S. F., Heck H., Hoppe P., Huth J., Ishii H., Kearsley A. T., Kissel J., Leitner J., Leroux H., Marhas M., Messenger K., Schwandt C. S., See T. H., Snead S., Stadermann F. J., Stephan T., Stroud R., Teslich N., Trigo-Rodríguez J. M., Tuzzolino A. J., Troadec D., Tsou P., Warren J., Westphal A., Wozniakiewicz P. J., Wright I. and Zinner E. 2006. Impact features on Stardust: Implications for comet Wild 2 dust. *Science* 314, 1716–1719.
- Ishibashi H., Arakawa M., Yamamoto J., Kagi H. 2012. Precise determination of Mg/Fe ratios applicable to terrestrial olivine samples using Raman spectroscopy. *J. Raman Spectroscopy* 43, 331 – 337.
- Ishii K. 1978. Lattice dynamics of forsterite. *Am. Min.* 63, 1198 – 1208.

- Kearsley A. T., Graham G. A., Burchell M. J., Cole M. J., Dai Z., Teslich N., Chater R. J., Wozniakiewicz P. J., Spratt J., and Jones G. 2007. Analytical scanning and transmission electron microscopy of laboratory impacts on Stardust aluminium foils: interpreting impact crater morphology and the composition of impact residues. *Meteoritics and Planetary Science* 42:191 – 210.
- Kearsley A.T., Burchell M.J., Price M.C., Graham G.A., Wozniakiewicz P.J., Cole M. J., Foster N.J. and Teslich N. 2009. Interpretation of Wild 2 dust fine structure: Comparison of Stardust aluminium foil craters to three dimensional shape of experimental impacts by artificial aggregate particles and meteorite powders. *Meteoritics and Planetary Science* 44, 1489 – 1510.
- Keller, L. P., Bajt, S., Baratta, G. A., Borg, J., Bradley, J. P., Brownlee, D. E., and Zolensky, M. 2006. Infrared spectroscopy of comet 81P/Wild 2 samples returned by Stardust. *Science*, 314(5806), 1728-1731.
- Kuebler, K. E., Jolliff, B. L., Wang, A. and Haskin, L. A. 2006. Extracting olivine (Fo–Fa) compositions from Raman spectral peak positions. *Geochimica et Cosmochimica Acta* 70(24), 6201-6222.
- Marsh S. P. 1980. LASL Shock hugoniot data. Los Angeles: University of California Press. 674 p.
- Melosh H. J. 1989. Impact cratering: A geologic process. Oxford: Oxford Univ. Press.
- Mohanani, K., Sharma, S.K., Bishop, F.C. 1993. A Raman spectral study of forsterite-monticellite solid solutions. *Am. Mineral.* 78, 42–48.
- Paques-Ledent M.Th, Tarte P. 1973. Vibrational studies of olivine-type compounds—I. The i.r. and Raman spectra of the isotopic species of  $Mg_2SiO_4$ . *Spectrochimica Acta Part A: Molecular Spectroscopy* 29, 1007 – 1016.
- Piriou, B., McMillan, P. 1983. The high-frequency vibrational spectra of vitreous and crystalline orthosilicates. *Am. Mineral.* 68, 426–443.
- Price, M. C., Kearsley, A. T., Burchell, M. J., Hörz, F., Borg, J., Bridges, J. C., Cole, M. J., Floss, C., Graham, G., Green, S.F., Hoppe, P., Leroux, H., Marhas, K.K., Park, N., Stroud, R., Stadermann, F.J. and Wozniakiewicz P.J. 2010. Comet 81P/Wild 2: The size distribution of finer (sub 10 micrometre) dust collected by the Stardust Spacecraft. *Meteoritics and Planetary Science* 45(9), 1409 – 1428.
- Price M. C., Kearsley A. T., and Burchell M. J. 2013. Validation of the Preston-Tonks-Wallace strength model at strain rates of  $10^{13} \text{ s}^{-1}$  for Al-1100, Tantalum and Copper using hypervelocity impact crater morphologies. *International Journal of Impact Engineering* 52, 1 – 10.
- Trigo-Rodríguez J., Domínguez G., Burchell M. J., Hörz F. and Lorca J. 2008. Bulbous tracks arising from hypervelocity capture in aerogel. *Meteoritics and Planetary Science* 43, 75 – 86.
- Wopenka, B. 2012. Raman spectroscopic investigation of two grains from comet 81P/Wild 2: Information that can be obtained beyond the presence of  $sp^2$ -bonded carbon", *Meteoritics & Planetary Science* 47(4), 565-584.
- Wozniakiewicz, P. J., Kearsley, A. T., Burchell, M. J., Foster, N. J., Cole, M. J., Bland, P. A., and Russell, S. S. 2009. In situ analysis of residues resulting from laboratory impacts into aluminum 1100 foil: Implications for Stardust crater analyses. *Meteoritics & Planetary science*, 44(10), 1541-1559.

Wozniakiewicz, P. J., Kearsley, A. T., Ishii, H. A., Burchell, M. J., Bradley, J. P., Teslich, N., Cole, M. J. and Price, M. C. 2012a. Stardust impact analogs: Resolving pre- and post- impact mineralogy in Stardust Al foils. *Meteoritics & Planetary Science* 47(4), 708-728.

Wozniakiewicz P. J., Kearsley A. T., Ishii, H. A., Burchell, M. J., Bradley, J. P., Teslich, N., Cole, M. J. and Price, M.C. 2012b. The origin of crystalline residues in Stardust Al foils: Surviving cometary dust or crystallized impact melts? *Meteoritics & Planetary Science* 47(4), 660-670.

Wozniakiewicz P.J., Ishii, H.A., Kearsley A.T., Bradley J.P, Price M.C., Burchell M.J., Teslich N., Cole M.J. 2015. *Meteoritics & Planetary Science* in press. doi: 10.1111/maps.12568

Xie X., Chen M., Dai C., El Goresy A., and Gillet P. 2001. A comparative study of naturally and experimentally shocked chondrites. *Earth and Planetary Science Letters* 187, 345–356.

Zolensky, M., Nakamura-Messenger, K., Rietmeijer, F., Leroux, H., Mikouchi, T., Ohsumi, K., Simon, S., Grossman, L., Stephan, T. and Weisberg, M. 2008. Comparing Wild 2 particles to chondrites and IDPs. *Meteoritics & Planetary Science* 43(1 – 2), 261-272.

## Figure Captions

**Figure 1:** Schematic of a typical Raman spectrum for an olivine grains, showing the distinct peak doublet labelled P1 and P2. Further peaks distinctive of olivine are also visible at higher wave numbers.

**Figure 2:** SEM back-scattered electron images of the olivine grains after milling.

**Figure 3:** Secondary Scanning Electron Microscope images of the foils and craters produce by each of the high speed ( $>1 \text{ kms}^{-1}$ ) shot. There is one shot per row. The image resolution increases from left to right from multiple to single craters.

**Figure 4:** The difference in wave number in the Raman spectra vs. impact speed between the residue in craters and the raw grains. (a) Peak P1, and (b) Peak P2.

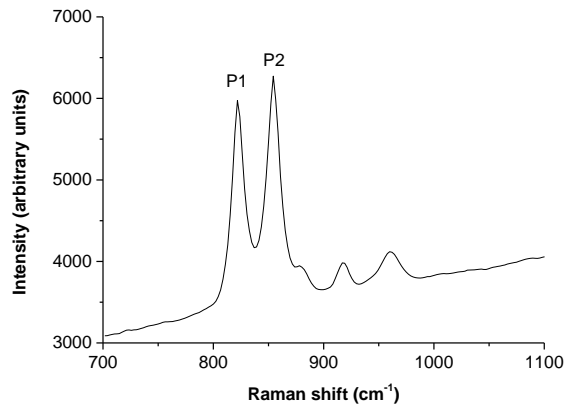
**Figure 5:** The difference in wave number in the Raman spectra vs. peak shock pressure between the residue in craters and the raw grains. (a) Peak P1, and (b) Peak P2.

**Figure 6: Mean Raman spectra from each shot showing the P1 and P2 peak position between  $800 \text{ cm}^{-1}$  and  $900 \text{ cm}^{-1}$ . The white circles show the position of the highest point on the P1 and P2 peak corresponding with the data in Table 1. The black lines show the position of the P1 and P2 raw olivine peaks so that the degree of shift can be observed in the spectra produced at different impact velocities.**

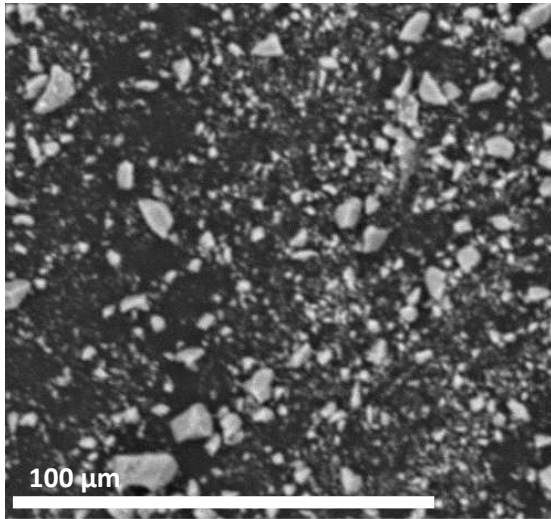
## Table captions

**Table 1:** Key shot data. This includes impact speed and peak shock pressures as well as the results of the Raman analyses for the mean positions of peaks P1 and P2. The subscript r indicates measurements made on crater residues, whilst a subscript o indicates measurements made on raw grains.

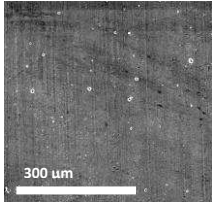
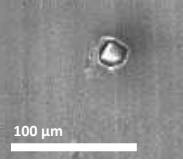
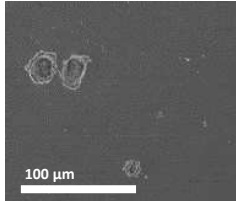
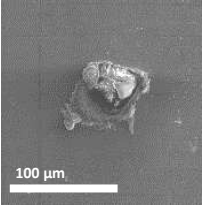
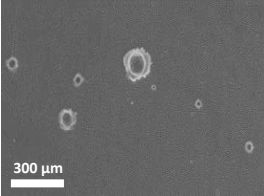
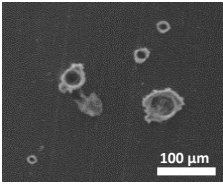
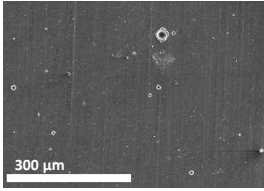
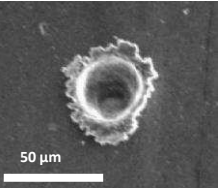
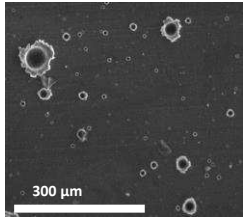
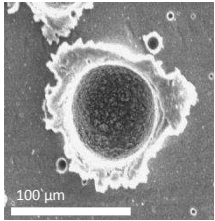




**Figure 1:** Schematic of a typical Raman spectrum for an olivine grains, showing the distinct peak doublet labelled P1 and P2. Further peaks distinctive of olivine are also visible at higher wave numbers.



**Figure 2:** SEM back-scattered electron images of the olivine grains after milling.

Foil #	Collection of craters	Single crater
A) G070714#1 1.09 kms <sup>-1</sup>		
B) G280514#2 1.9 kms <sup>-1</sup>		
C) G270514#1 4.0 kms <sup>-1</sup>		
D) G260615#2 5.2 kms <sup>-1</sup>		
E) G020414#1 6.3 kms <sup>-1</sup>		

**Figure 3:** Secondary Scanning Electron Microscope images of the foils and craters produce by each of the high speed (>1 kms<sup>-1</sup>) shot. There is one shot per row. The image resolution increases from left to right from multiple to single craters.

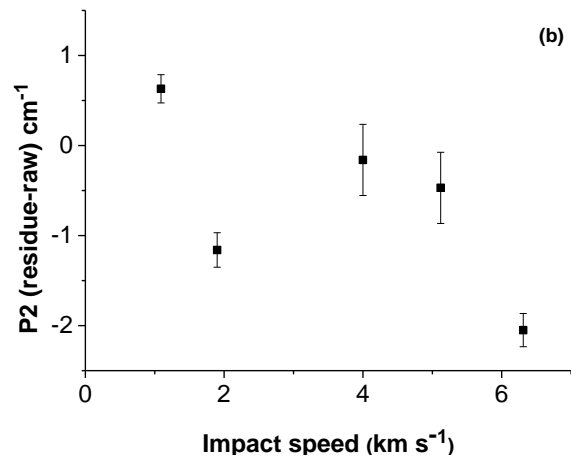
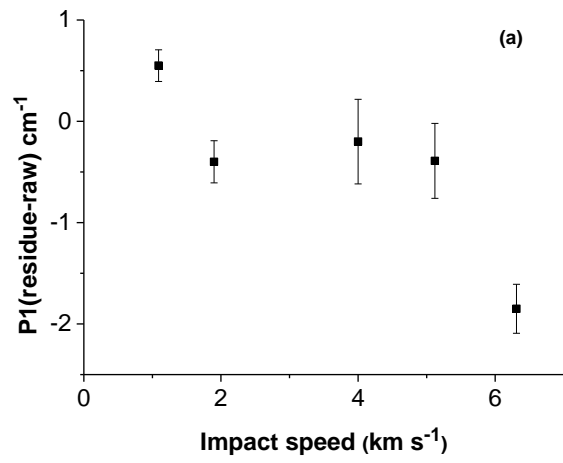


**Figure 4:** The difference in wave number in the Raman spectra vs. impact speed between the residue in craters and the raw grains. (a) Peak P1, and (b) Peak P2.

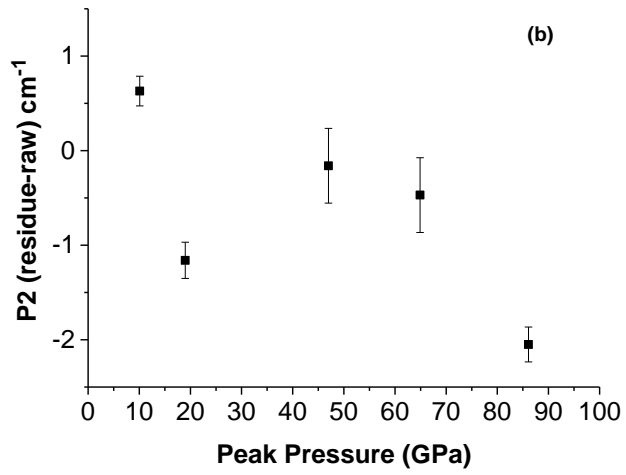
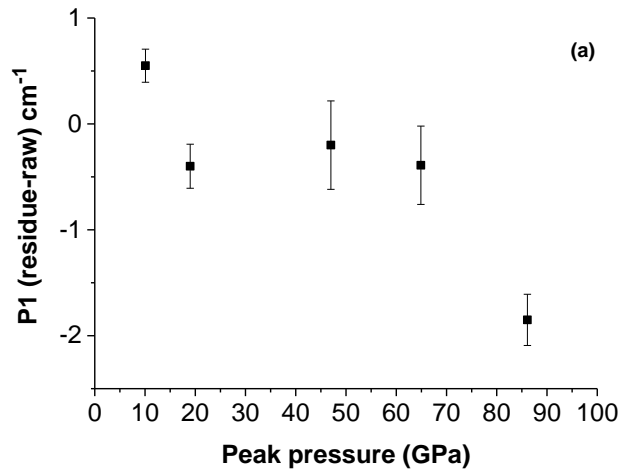


**Figure 5:** The difference in wave number in the Raman spectra vs. peak shock pressure between the residue in craters and the raw grains. (a) Peak P1, and (b) Peak P2.

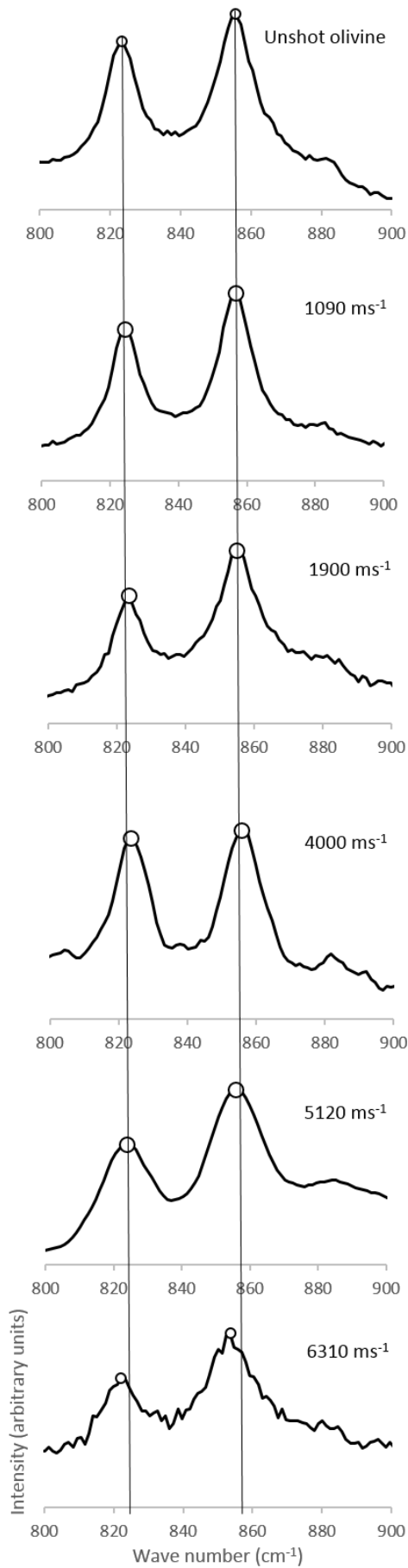


**Figure 6:** Mean Raman spectra from each shot showing the P1 and P2 peak position between 800 cm<sup>-1</sup> and 900 cm<sup>-1</sup>. The white circles show the position of the highest point on the P1 and P2 peak corresponding with the data in Table 1. The black lines show the position of the P1 and P2 raw olivine peaks so that the degree of shift can be observed in the spectra produced at different impact velocities.

**Table 1:** Key shot data. This includes impact speed and peak shock pressures as well as the results of the Raman analyses for the mean positions of peaks P1 and P2. The subscript r indicates measurements made on crater residues, whilst a subscript o indicates measurements made on raw grains.

Velocity (ms <sup>-1</sup> )	Peak Pressure (GPa)	Residue (cm <sup>-1</sup> )					Peak shift (cm <sup>-1</sup> )		n
		P1 <sub>r</sub>	σ	P2 <sub>r</sub>	σ	P2 <sub>r</sub> -P1 <sub>r</sub>	P1 <sub>r</sub> -P1 <sub>o</sub>	P2 <sub>r</sub> -P2 <sub>o</sub>	
600	5.3	n/a	n/a	n/a	n/a	n/a	n/a	n/a	n/a
1090	10.1	824.35±0.10	0.20	856.64±0.07	0.13	32.29	0.6	0.6	4
1900	19.0	823.40±0.17	0.66	854.85±0.13	0.52	31.45	-0.4	-1.2	15
4000	47.0	823.60±0.40	1.27	855.85±0.37	1.18	32.25	-0.2	-0.2	10
5120	64.9	823.81±0.35	1.12	855.93±0.37	1.17	32.12	-0.4	-0.5	10
6310	86.1	821.95±0.21	0.62	853.96±0.21	0.63	31.02	-1.9	-2.0	9